




Computational Fluid Dynamics Analysis of Effect of Braking Plate Configurations on the Aerodynamic Behaviors of an Ahmed Car

Fujian Jiang¹ · Jiqiang Niu^{1,2,3}  · Rui Li^{4,5} · Yueming Wang^{1,3} · Yingchao Zhang²

Received: 22 October 2021 / Accepted: 10 November 2022 / Published online: 22 November 2022
© The Author(s), under exclusive licence to Springer Nature B.V. 2022

Abstract

Braking distance, particularly the emergency braking distance at high speed, is essential to ensuring safety. Aerodynamic drag and negative lift can be effectively increased by setting up a plate at the rear of the car, thus improving the grip of the tires and reducing the braking distance. The Ahmed car model was selected for the numerical simulation. The aerodynamic behavior of the car with different configurations of plates at different opening angles was simulated using an improved delayed detached eddy simulation based on the shear stress transfer $k-\omega$ turbulence model, and the numerical method used in this study was verified using wind tunnel tests. Results showed that the upstream plate is optimal for increasing the car aerodynamic braking performance and noticeably reduces the fluctuation in aerodynamic forces. The aerodynamic drag is more sensitive to the installation position of the plate than aerodynamic lift. The aerodynamic forces on the car body and plate increase as the opening angle and size increase (except for the aerodynamic lift of a car body with a downstream plate), and the greatest effect is on the car body. Aerodynamic braking distance decreases as the opening angle and size of the plate increase, especially for the upstream plate. The optimal opening angle of the downstream plate is approximately 70° , and the braking effect is not significantly because of the small downstream plate.

Keywords Ahmed car · Braking plate · Braking distance · Aerodynamic performance · Computational fluid dynamics

✉ Jiqiang Niu
jiqiang_niu@163.com

¹ School of Mechanical Engineering, Southwest Jiaotong University, Chengdu 610031, Sichuan, China

² State Key Laboratory of Automotive Simulation and Control, Jilin University, Changchun 130025, Jilin, China

³ Technology and Equipment of Rail Transit Operation and Maintenance Key Laboratory of Sichuan Province, Chengdu 610031, Sichuan, China

⁴ School of Mechanical Engineering, Lanzhou Jiaotong University, Lanzhou 730070, Gansu, China

⁵ Birmingham Centre for Railway Research and Education, University of Birmingham, Birmingham B15 2TT, UK

1 Introduction

Long downhill roads are characteristic of mountainous areas, requiring vehicles to be in a braking state for extended durations. The working state of the brake disc can be severely affected by thermal stress, which may cause braking failure and threaten safety while driving. As the running speed of a car increases, the safety requirements of the car also increase and the aforementioned phenomenon is exacerbated (Hucho and Sovran 1993). It is important to minimize the braking distance in emergency braking situations that involve high-speed operation to ensure the safety of the car and its riders (Kudarauskas 2007). To strengthen the general braking ability, it is also necessary to incorporate modern braking technology. Previous studies found that an aerodynamic plate—widely used in sports cars and trains—can effectively change the vehicle aerodynamic performance (McKay and Gopalathnam 2002; Katz 2006; Niu et al. 2021a; Zuo et al. 2014). The effect of aerodynamic braking increases with increasing running speed (Devanuri 2018). Therefore, an aerodynamic brake for car braking is proposed in this study.

Niu et al. (2020a) analyzed the effects of serially arranging small plates and those of a single large plate (with the same windward area) on flow field and aerodynamic drag. They found that small plates are series exhibited better aerodynamic braking performance. The train-car connection is a major source of aerodynamic drag in trains (Niu et al. 2019). Niu et al. (2021b) placed a plate in this region to analyze the effect of the installation position (car-connecting part vs. uniform body) on the train aerodynamic performance. They found that the plate installed on the train uniform body improved aerodynamic performance, but significantly disturbed the surrounding flow field. A study on the effect of three types of plates (upstream large plate, downstream large plate, and upstream and downstream small plates) installed at the car-connection on aerodynamic braking performance in trains showed that the large plate placed downstream of the car-connection part yielded optimal braking. Further, the pantograph and air-conditioning unit should be arranged away from the plate (Niu et al. 2020b). Niu et al. (2021c) analyzed the interaction between two adjacent plates, and observed that opening the downstream plate attenuated the braking effect and emphasized the importance of the distance between adjacent plates. It was found that rapidly opening the plate disrupts the flow field balance around the train, thus threatening safety. Zhai et al. (2020) found that the aerodynamic force and pressure field downstream of the plate forms a large aerodynamic pulse in the opening stage of the plate, and the crosswind environment further increases the aforementioned aerodynamic pulse.

Scholars have recently studied the braking effect of plates and the effect of aerodynamic plates on the car aerodynamic performance. Devanuri (2018) studied the effect of the position, height, and angle of a plate on the aerodynamic drag of a car. The author determined influential laws and used the Taguchi-ANOVA technique to identify the set of parameters with the largest aerodynamic drag. However, the location of the plate was limited to the car roof and excluded the back bevel of the car. Broniszewski and Piechna (Devanuri 2018) investigated the impact of unsteady aerodynamic loads on car dynamics with a tail plate using ANSYS/Fluent software and MSC Adams Car software. They found that installing the tail plate reduced the stopping distance by approximately 6% (at an initial braking speed of 40 m/s). Kurec et al. (Broniszewski and Piechna 2019; Kurec et al. 2019a) studied the effect of both the position and angle of the plate and spoiler on the aerodynamic behavior of a sports car, and found that the combination of plate and spoiler could effectively improve aerodynamic drag, that small active aerodynamic elements (such as profile vane and side plates) could indirectly increase braking force, and that the braking distance

could be reduced by up to 31% (at an initial braking speed of 200 km/h). The evolution of the flow field around a car with a plate at different angles, and its effect on car aerodynamic behavior and braking distance has not been studied yet. Current research on vehicle aerodynamic braking is focused on the rear wing of the racing car. Controlling the wake to increase the vehicle aerodynamic drag and the contact force between the rear wheel and ground can slow the vehicle and control its attitude.

In this study, an Ahmed car with a plate mounted on a slanted back was set up, and the unsteady aerodynamic behaviors of the car for different installation positions, as well as plate dimensions and opening angles were analyzed. This study aims (i) to explain the braking effect of a plate installed on the slanted back of a car (ii) to understand the unsteady evolution of the flow field around the car in the presence of the plate, and (iii) to investigate the effects of installation position, opening angle, and plate dimensions on flow field and braking performance, which can assist engineers in designing a braking plate. An introduction on model geometry of car and plate is presented in Sect. 2. The setups for computational fluid dynamics are introduced in Sect. 3 and include a turbulence model, and data postprocessing. The validation of the simulation approach, including the grid resolution analysis and comparison with a wind tunnel test, is presented in Sect. 4. The results and discussions are presented in Sect. 5. Finally, the key conclusions are presented in Sect. 6.

2 Description of Models

The Ahmed car model, which represents the geometry of a generic car, has been widely tested in previous studies (Kurec et al. 2019b; Ahmed et al. 1984; Lienhart and Becker 2003), and it was selected as the numerical model for this study. The flow features around this simplified resemble those of a real car (Thacker et al. 2013, 2012; Fares 2006; Guilmineau 2008; Minguez et al. 2008). The back is slanted at 25° because the counter-rotating vortices are strong enough to introduce momentum into the separation region to reattach the flow halfway down the slanted back, which has been widely used in wind tunnel tests (Serre et al. 2013; Ashton and Revell 2015; Rao et al. 2018). As shown in Fig. 1,

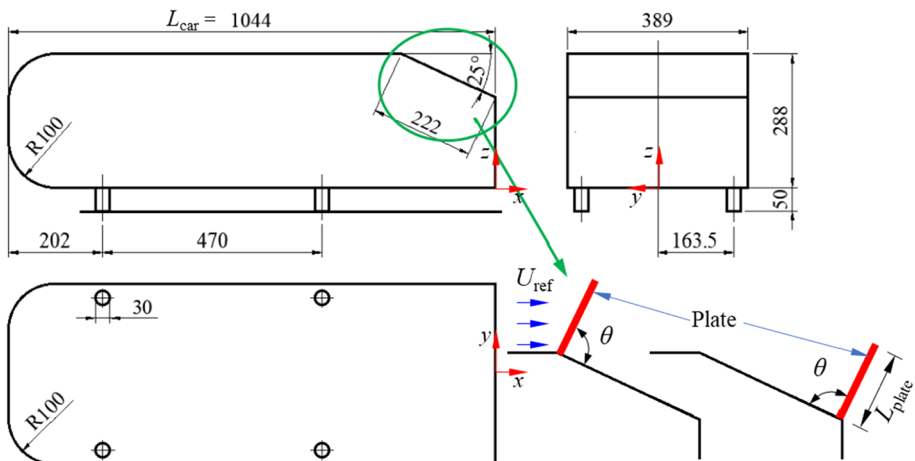


Fig. 1 Dimensions of the Ahmed car model with and without an aerodynamic braking plate (unit: mm)

dimensions of the Ahmed car model—a 1/5th full-scale car model—are detailed: the length, width and height of the car model are 1044 mm, 389 mm, and 338 mm, respectively. To enhance car braking performance, an aerodynamic braking plate was installed on the slanted side edge of the car. As shown on the lower right of Fig. 1, there are two ways of installing the plate: one on the upper edge of the slanted back and the other on the lower edge of the slanted back. The opening angles (between the plate and slanted back of the car, θ) of the plate were 0° , 30° , 60° , and 90° . To study the effect of plate dimensions, the lengths of the plate (L_{plate}) were considered to be variables: 55.5 mm, 111 mm, 166.5 mm, and 222 mm, the corresponding plate area (S_{plate}) is 0.022 m^2 , 0.043 m^2 , 0.065 m^2 , and 0.086 m^2 , respectively. Further, the width of the plate was similar to that of the Ahmed car model, and the thickness of the plate was 7 mm. The running speed of the car is the speed of incoming airflow U_{ref} , which is 40 m/s. To reduce grid cells to meet our computing performance, the full model and symmetrical model are both adopted in this study: The full model with supports is used in Sect. 4, which are mainly for comparison with the experimental data to verify the reliability of the numerical settings. Considering that results in Sect. 5 are obtained based on the symmetric model, the symmetrical model is used in Sect. 4 to ensure the reliability of the selected grid resolution.

3 Numerical Setups

3.1 Numerical Method

The numerical simulation of the flow field around the car with the braking plate was based on the inertial Cartesian coordinate system, and the unsteady N-S equations in integral form can be expressed as follows:

$$\frac{\partial}{\partial t} \iiint_{\Omega} \hat{Q} dV + \iint_S \hat{\mathbf{F}} \cdot \mathbf{n} \cdot dS = \iint_S \hat{\mathbf{F}}^v \cdot \mathbf{n} \cdot dS \quad (1)$$

where V is the control volume, S is the boundary of the control volume, and \mathbf{n} is the external normal unit vector of microelement. The above equation is discretized by the finite volume method. The flow field analysis was based on the full turbulence assumption, the $k-\omega$ SST two equation turbulence model was used for turbulence numerical simulation, and the double time iterative method was used for time advance.

To describe the multiscale and unsteady characteristics of turbulence without incurring the cost associated with large-scale computing methods, such as direct numerical simulation, the large eddy simulation (LES) method was considered. However, this method is expensive and time consuming. Reynolds-averaged Navier–Stokes equations (RANS) are also effective for solving the engineering problem. However, RANS only provides the average turbulence value, which is insufficient for predicting unsteady flow. Therefore, a RANS/LES hybrid model was proposed to improve the accuracy and efficiency (Liang et al. 2020; Spalart 1997; Spalart et al. 2006; Menter and Kuntz 2004). Further, improved delayed detached eddy simulation (IDDES) was incorporated, which has been widely used in vehicle aerodynamics. IDDES, a type of the RANS/LES hybrid method, method adopts different calculation methods for different regions of the flow field. In the region dominated by vortex motion in the flow field, the (delayed detached eddy simulation) DDES method is used, whereas the wall function model of the LES

(WMLES) method is used in the boundary layer near the model surface, to better simulate the velocity distribution of the boundary layer. This eliminates the “log layer mismatch” problem caused by the using the DDES method in the boundary layer. IDDES method combines the advantages of the DDES and WMLES methods. Compared with other DES methods (Menter and Kuntz 2004; Travin et al. 2002), IDDES exhibits strong simulation ability for small separation flow. IDDES differs from DDES with respect to two main modifications (Xiao and Fu 2009): in redefining the grid scale and constructing a new hybrid function of RANS and LES methods. These two aspects are introduced below.

As defined in IDDES, the grid scale (Δ) considers the size of the grid and introduces the effect of model surface distance. The expression is as follows:

$$\Delta = \min \{ \max [C_w d_w, C_w h_w, h_{wn}], h_{\max} \} \tag{2}$$

where d_w is the model surface distance, h_{\max} is the maximum scale of the grid element in the three directions, h_{wn} is the local grid scale in the normal direction of the model surface, and C_w is the constant, which is considered to be 0.15.

In IDDES method, a new turbulence length scale l_{IDDES} is reconstructed, which is expressed as follows:

$$l_{IDDES} = f_{hyb} (1 + f_{restore}) l_{RANS} + (1 - f_{hyb}) C_{DES} \Delta \tag{3}$$

IDDES hybrid model was formed by replacing the turbulence length scale l_{IDDES} defined in the above formula with the one in $k-\omega$ SST Turbulence model.

In formula (3), the mixed function f_{hyb} includes both DDES and WMLES branches, and it is constructed as follows:

$$f_{hyb} = \max \{ (1 - f_d), f_{step} \} \tag{4}$$

where f_d is the delay function in DDES method, and expressed as follows:

$$f_d = 1 - \tanh \left[(8r_d)^3 \right]$$

$$r_d = \frac{1}{k^2 d_w^2} \cdot \frac{v_t}{\max \left\{ \left[\sum_{ij} (\partial u_i / \partial x_j)^2 \right]^{0.5}, 10^{-10} \right\}}$$

Here, f_{step} only works when the WMLES model is called; thus, RANS is quickly replaced with LES in the boundary layer, and it is expressed as follows:

$$f_{step} = \min \{ 2 \exp(-9\alpha^2), 1.0 \} \tag{5}$$

where α is expressed as $0.25 \cdot d_w / h_{\max}$, and f_{step} can make the RANS method quickly convert to LES in the region of $0.5275 < d_w / h_{\max} < 1.0$.

$$f_{restore} = \max \{ (f_{hill} - 1), 0 \} f_{amp} \tag{6}$$

where f_{hill} is expressed as follows:

$$f_{hill} = \begin{cases} 2 \exp(-11.09\alpha^2), & \alpha \geq 0 \\ 2 \exp(-9.0\alpha^2), & \alpha < 0 \end{cases}$$

In formula (6), the form of function f_{amp} is expressed as follows:

$$f_{amp} = 1.0 - \max\{f_t, f_l\} \quad (7)$$

where f_t and f_l are expressed as follows:

$$\begin{aligned} f_t &= \tanh\left[(c_t^2 r_d)^3\right] \\ f_l &= \tanh\left[(c_l^2 r_{dl})^{10}\right] \\ r_{dl} &= \frac{1}{k^2 d_w^2} \cdot \frac{v_l}{\max\left\{\left[\sum_{ij} (\partial u_i / \partial x_j)^2\right]^{0.5}, 10^{-10}\right\}} \end{aligned}$$

where k and c_t are constant: $k=0.41$ and $c_t=1.87$.

A pressure-based solver in commercial software FLUENT was used for all calculations. A bounded second-order implicit scheme format was applied to address the dual time step. Both convection and diffusion terms were discretized using the bounded central differencing scheme and second-order upwind scheme, respectively. The pressure–velocity coupling was resolved using the semi-implicit pressure-linked equation-consistent algorithm. The physical time step and iteration for each time step were 0.5×10^{-4} s and 30, respectively, and the residuals for each equation were less than 10^{-4} for each time step. For all calculations, the calculation time was approximately 2.0 s, which is approximately 80 times the time taken for airflow to pass through the car model.

3.2 Grid Generation

OpenFOAM, an open source software for computational fluid dynamics (CFD), was used in grid generation, and snappyHexMeshDict was selected to generate hexahedral mesh around the car model. To determine the appropriate grid resolution, three grid densities were generated, and the grids on the surface of car model with plate for the three grid resolutions is shown in Fig. 2. The tangential dimension of grid on surface of the scaled car body generated by the coarse, medium and fine grid are 3.13 mm, 1.56 mm and 0.78 mm, respectively, and grids on the surface of plate are one level higher than the grids on the surface of car body. Figure 3a and b show that there are four refinement boxes around the car model; their dimensions are $10 \text{ m} \times 0.8 \text{ m} \times 0.7 \text{ m}$ (Region-1), $10 \text{ m} \times 0.6 \text{ m} \times 0.6 \text{ m}$ (Region-2), $1.0 \text{ m} \times 0.5 \text{ m} \times 0.5 \text{ m}$ (Region-3) and $1.6 \text{ m} \times 0.5 \text{ m} \times 0.1 \text{ m}$ (Region-4), and the size of corresponding cells are 6.25 mm (Region-1), 12.5 mm (Region-2), and 3.125 mm (Region-3 and Region-4), respectively. The three grids only differed in the grid dimensions on the model surface; other parameters (e.g., the position and dimensions of refinement boxes) were the same. A shown in Fig. 2c, ten layers grids were added to the boundary layer to simulate the flow field close to the surface of the car body, and the first layer was set as approximately 1.56×10^{-2} mm to ensure that y^+ was less than 1 for all near-wall cells around the car model.

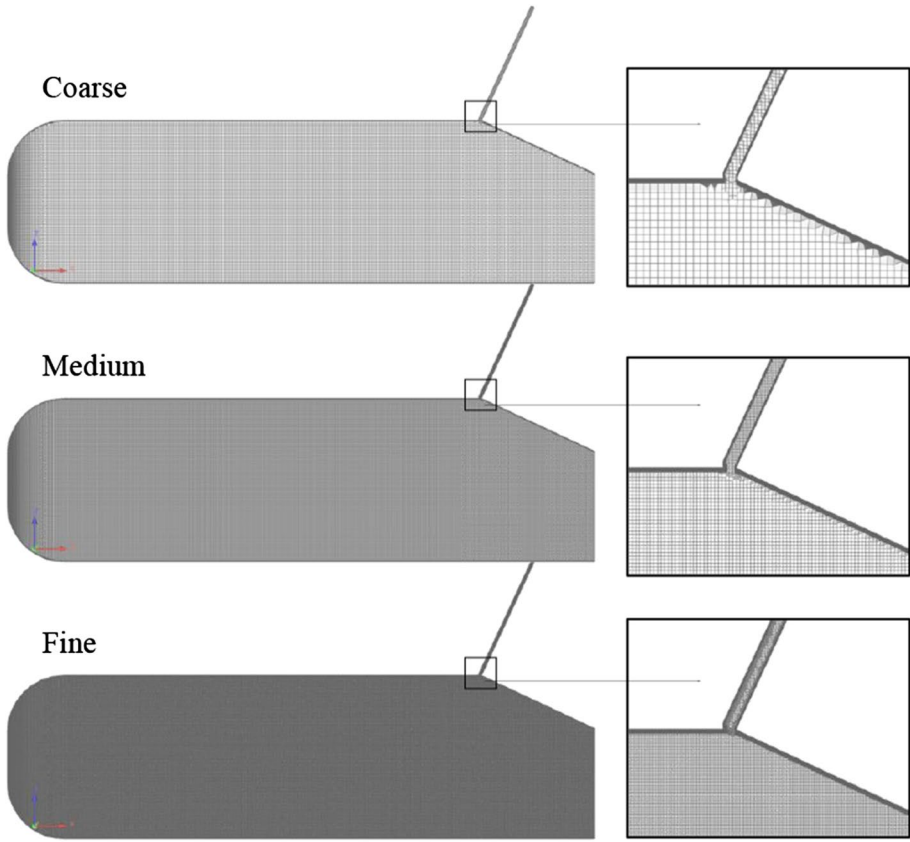


Fig. 2 Surface grids of car model with plate for grid resolutions

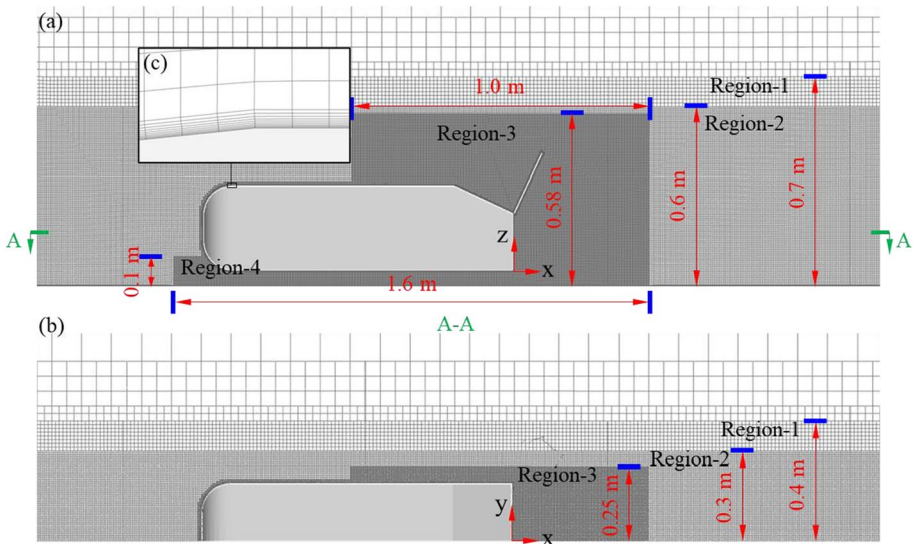


Fig. 3 Top **a**, side **b** and local **c** views of hexahedral mesh around the Ahmed car model

3.3 Computational Domain

A schematic of the computational domain for the scaled car model is presented in Fig. 4; the length, width, and height of the domain are $29.6 H$, $12.0 H$, and $7.5 H$, respectively, where H is the height of the car model. To compare with the experimental data shown in Sect. 4, the full computational domain for the car model without plate is adopted; To reduce the costs of calculations, the symmetrical computational domain is used in the study on effect of plate presented in Sect. 5, the symmetrical model has been widely used in Ahmed car (Corallo et al. 2015; Mohammadikalakoo et al. 2020), and the flow field around the Ahmed car with plate is almost symmetrical based on our previous calculation. As previously defined (Ahmed et al. 1984; Gritskevich et al. 2016; Ashton et al. 2016), the upstream (red line) and downstream (blue line) surfaces are the velocity inlet ($U_{ref} = 40$ m/s, with a turbulent viscosity ratio of 20 and a turbulent intensity of 1%) and the pressure outlet with a reference pressure of 0 Pa. The Reynolds number for the flow field is approximately $Re = 8.22 \times 10^5$ based on the height of the car model. The two sides and the upper surfaces are defined as slip walls with a slip speed of 40 m/s, and the lower surface is defined as a no-slip wall to match the experiment with non-slip ground. The car model is located at $8 H$ downstream of the inlet boundary condition (red line), and the length of the region behind the car model is more than $18 H$, which is long enough to allow the full development of a wake.

3.4 Description of the Data Postprocessing

For convenient comparison and analysis, the aerodynamic drag (F_z), aerodynamic lift force (F_y), and pressure (p) were nondimensionalized as follows:

$$C_{x,z} = \frac{F_{x,z}}{0.5\rho U_{ref}^2 S_{car}} \tag{8}$$

$$C_p = \frac{p - p_0}{0.5\rho U_{ref}^2} \tag{9}$$

u , v , and w are velocity in three directions of x , y and z , respectively. ν_t and ν are molecular and turbulent viscosity, respectively. κ is the von Kármán constant of 0.4. d is the distance to the wall.

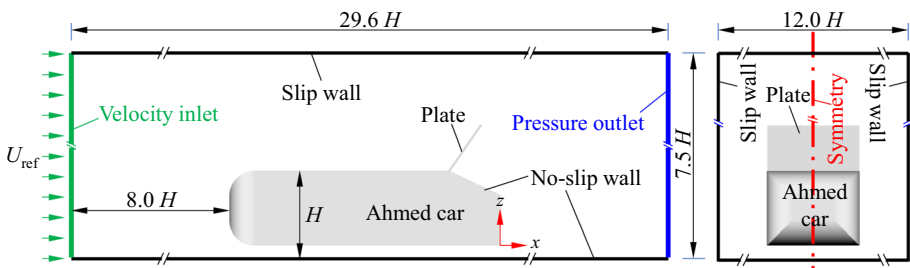


Fig. 4 Dimensions and boundary conditions of the computational domain

where ρ is the air density of 1.225 kg/m^3 ; S_{car} , the cross-sectional area of the full-scale uniform car body, $0.389 \times 0.288 \text{ m}^2$ here; p_0 is the reference pressure (0 Pa in this study); and C_x , C_z , and C_p are the aerodynamic drag coefficient, aerodynamic lift force coefficient, and pressure coefficient, respectively. Considering the effect of periodic vortex shedding in the flow field on aerodynamic characteristics of the car, the results used in the following analysis are the average values after the full development of the flow field around the car. For the unsteady calculation, the sampling time starts from 0.5 s and lasts for about 1.5 s.

To realize the visualization of flow field, some parameters are defined as follows:

$$f_d = 1 - \tanh([8r_d])^3 \quad (10)$$

$$r_d = \frac{\nu_t + \nu}{\sqrt{u^2 + v^2 + w^2} \kappa^2 d^2} \quad (11)$$

$$\text{Swirl} = \frac{\Omega \cdot \bar{U}}{\rho \bar{U}^2} \quad (12)$$

u , v , and w are velocity in three directions of x , y and z , respectively. ν_t and ν are molecular and turbulent viscosity respectively, they can be export from Fluent. κ is the von Kármán constant of 0.4. d is the distance to the wall. Ω is vorticity, which can be export from Fluent. \bar{U} is the mean velocity of flow field.

4 Approximation and Comparison

To verify the accuracy and reliability of the numerical settings introduced in Sect. 3.1, the aerodynamic forces and flow around the Ahmed car without a plate generated by three set of grid resolutions were compared with experimental results sourced from previous studies (Kurec et al. 2019b; Guilmineau 2018; Conan et al. 2011; Joseph et al. 2012; Krajnović and Davidson 2005a, 2005b; Rossitto et al. 2016). It should be noted that the calculation model in this section is not symmetrical, and the bottom of the model is equipped with four supports to be consistent with the experiment. The grid generation used in this section is basically same as the one presented in Sect. 3.2. As shown in Table 1, the numerically simulated C_x of the car model without plate was within the range of the experimental values obtained from several tests, and the difference between the medium C_x and fine grid resolutions for the car without plate was less than 0.8%. Generally, it was difficult to accurately simulate the aerodynamic lift force; the difference between the C_z value of the medium and fine simulations for the car without plate was approximately 8% and higher than the test values, with differences exceeding 10%. This was mainly because the flow field at the bottom of the car is complex caused by the four supports under the car, and the space under the car and ground conditions in the experiment was not necessarily the same as that in the simulation.

The mean streamwise velocity profiles obtained from numerical simulations and wind tunnel test are shown in Fig. 5 to intuitively compare the differences among the three grid resolutions. Differences among the mean streamwise velocity distributions in the three grid resolutions can be observed. The medium grid resolution is very close to the fine grid resolution, and their distributions are consistent with the test data; however, the coarse grid

Table 1 Grid parameters for the three grid resolutions for the Ahmed car without plate and with supports, and their numerically simulated mean aerodynamic force coefficients compared with experimental data

Numerical simulation				Experiment (Kurec et al. 2019b; Guilmineau 2018; Conan et al. 2011; Joseph et al. 2012)
Item	Coarse	Medium	Fine	–
Thickness of first boundary layer (mm)		0.0156		
Number of boundary layer and its growth factor		10 and 1.2		
Dimensions of grids on the model surface (mm)				
Car body	3.13	1.56	0.78	
Dimensions of grids in regions of 1, 2, 3 and 4 (mm)	12.5, 6.25, 3.125 and 3.125			
Total number of grid cells (million)	6.39	16.56	23.03	
C_x	0.3424	0.3190	0.3167	0.298, 0.312, 0.343, 0.356
C_z	0.0795	0.3401	0.3679	0.311

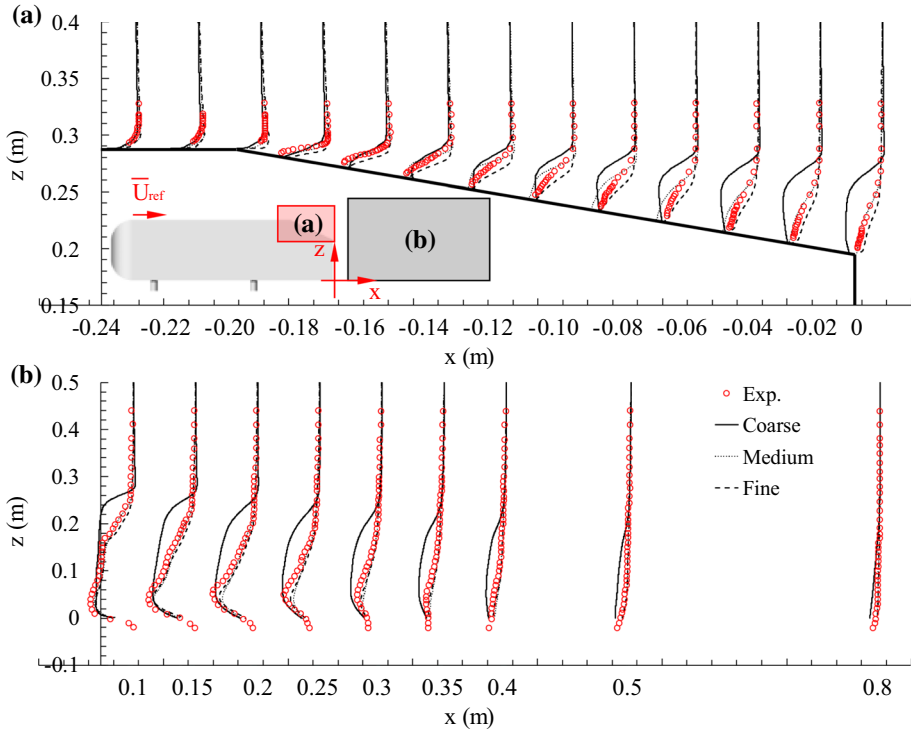


Fig. 5 Comparison of the mean streamwise velocity profiles above the slanted back **a** and behind **b** Ahmed car body corresponding to the wind tunnel test (Ashton and Revell 2015) and numerical simulation with different grid resolutions on a symmetrical plane

resolution is distinctive, especially near the rear. As shown in Fig. 5, for the numerical results there is a significant difference from the coarse to medium and fine grids, for most areas of the slant back of car, the mean velocity profiles for the coarse grid are particularly far from the experimental values. The level of turbulence over the rear slant back of the car is initially under-predicted such that there is very little modelled or resolved turbulence in this region. The consequence of this under-prediction of the turbulence level is to have almost no turbulent mixing, and as a result the flow stays completely separated over the rear slant. Around the separated flow over the rear slant, the modelled turbulence would be expected to be low and the resolved turbulence level high. If the grid is too coarse, the separated shear layer does not generate resolved content, but as it is in LES mode the turbulence viscosity ratio is computed to be very low. For the coarse grid this is very clearly observed from plots of mean turbulence kinetic energy (TKE) (modelled+resolved components) are plotted in Fig. 6, which shows that the three grid resolutions fail to correctly predict the level of turbulence at the point of separation. Significantly, it can be seen from Fig. 6 that there is a large under-prediction of TKE at the centreline versus the experiment, especially the middle of the car slant back. The grid resolution also has great effect on the distribution of TKE, but the regularity is obvious. With the increase of the grid density on the car body, the maximum value of TKE appears close to the car body, which is consistent with the situation in the study of Ashton and Revell (Ashton and Revell 2015). The

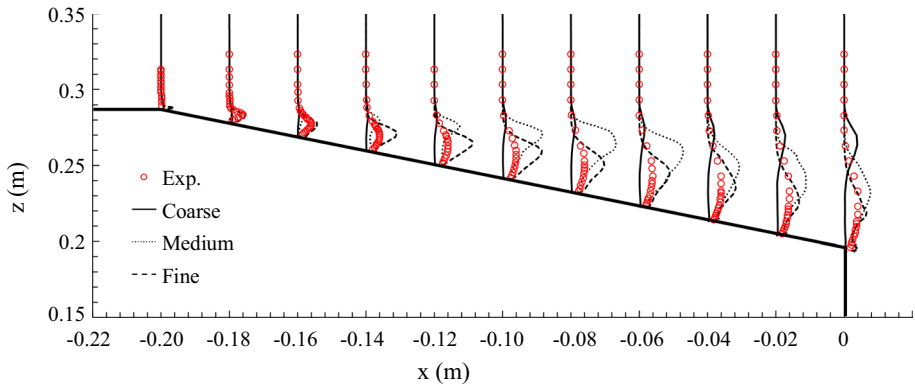


Fig. 6 Comparison of the mean turbulent kinetic energy (TKE) profiles above the slanted back of Ahmed car body corresponding to the wind tunnel test (Ashton and Revell 2015) and numerical simulation with different grid resolutions on a symmetrical plane

above analysis suggests that the data obtained using the medium grid resolution is accurate enough, validating the reliability of the conclusions.

5 Results and Discussion

The effects of the installation positions of the plate (plate arranged at upstream and downstream of the car slant back) on the unsteady aerodynamic performance of the car are first compared and analyzed in Sect. 5.1. The effect of the opening angle and size on car aerodynamic performance is analyzed in Sect. 5.2, and the aerodynamic braking distance of the car under the action of aerodynamic plate is estimated in Sect. 5.3 based on the results presented in Sect. 5.2.

5.1 Effect of Plate Position on Aerodynamic Behaviour of Ahmed Car

Aerodynamic coefficients of the car with plates with full length (L_{plate}) at an opening angle of 90° and arranged in the upstream and downstream of slanted back of the car body (Ahmed car without plate), namely upstream plate and downstream plate, are obtained; they are presented in Table 2. Table 2 shows that the C_x and C_z of the car body and plate in a car with upstream plate are significantly greater than those of the car with a downstream plate: C_x of the car body and plate increased by 55% and 15%, respectively, and the C_z of the car body and plate in a car with upstream plate increased by 23% and 10%, respectively. Therefore, the C_x is sensitive to the installation position of the plate with respect to the C_z , and the upstream plate is optimal for increasing the car aerodynamic braking performance. Standard deviation, which can be used to describe the fluctuation in aerodynamic force, has been widely used in previous studies. As listed in Table 2, compared with the case of downstream plate, the fluctuation in the aerodynamic forces of both car body and plate in a car with a downstream plate is effectively reduced. Relative to the one of downstream plate, the standard deviation of the C_x and C_z of the car body with upstream plate decreases by approximately 30% and 67% respectively, and the standard deviation of aerodynamic

Table 2 Mean and standard deviation values of aerodynamic force coefficients for the Ahmed car model without supports and with upstream or downstream plate with full length (L_{plate}) at the full opening angle ($\theta=90^\circ$). (difference, defined as the ratio of the difference between the cars with downstream and upstream plate to the one of downstream plate)

Values	Object	Aerodynamic coefficients	Without plate	Downstream plate	Upstream plate	Difference (%)
Mean	Car body	C_x	0.2827	0.4624	0.7184	55.36
		C_z	0.2506	-0.7982	-0.9874	23.70
	Plate	C_x	-	0.7091	0.8211	15.79
		C_z	-	-0.3292	-0.3629	10.24
Standard deviation	Car body	C_x	0.0081	0.0315	0.0219	-30.48
		C_z	0.0290	0.0792	0.0259	-67.30
	Plate	C_x	-	0.0954	0.0168	-82.39
		C_z	-	0.0449	0.0075	-83.30

coefficients for the upstream plate decreases by more than 83%; that is, the fluctuation degree of the aerodynamic coefficients of the plate is more sensitive to the installation position of the plate. The above analysis indicate that the upstream plate significantly improves aerodynamic forces and reduces the fluctuation in aerodynamic forces.

As shown in Fig. 7a, airflow flows through the car body and forms some small vortices around the car, especially around the corner of the car. The airflow near the rear of the car is relatively disordered, as it moves away from the car, airflow in the wake rectifies into a large vortex. Figure 7b and c show that flow downstream the car is significantly affected by the plate, the range of low-speed zone is significantly expanded, especially the upstream plate, which can also explain that the aerodynamic drag of the car with an upstream plate is larger than that of downstream plate. The flow field downstream the car is disturbed by the plate, range of the vortices are increased, and the position of the vortices is raised. Consequently, the vortices behind the car with a downstream plate are positioned lower than in the car with an upstream plate. The airflow distribution around the car was clearly shown in Fig. 8, which is consistent with Fig. 7. The disturbance of the upstream plate on the wake is significantly greater than that of the downstream plate.

Considering that the unsteady flow around the plate is easy to cause flow-induced vibration, the power spectral density (PSD) of aerodynamic force coefficients is obtained and analyzed. As shown in Fig. 9a, PSD of C_x of the car body is increased by plate, especially downstream plate, which means that vortices around the car is strengthened by plate, and this is consistent with what is observed in Fig. 8. Figure 9b shows that PSD of C_z of the car body is also increased by plate, and the effect of upstream and downstream plates are basically the same. Figure 9a and b also show that dominant frequency of C_x is significantly affected by plate, dominant frequency of C_x of the car is increased a lot by downstream plate; dominant frequency of C_z of the car basically is not affected by plates. Figure 9c and d show that PSD of both C_x and C_z of the downstream plate is bigger than that of upstream plate, the dominant frequency of C_x and C_z between downstream and upstream plates are close. Therefore, the natural frequency design of the plate device needs to consider avoiding the above frequencies.

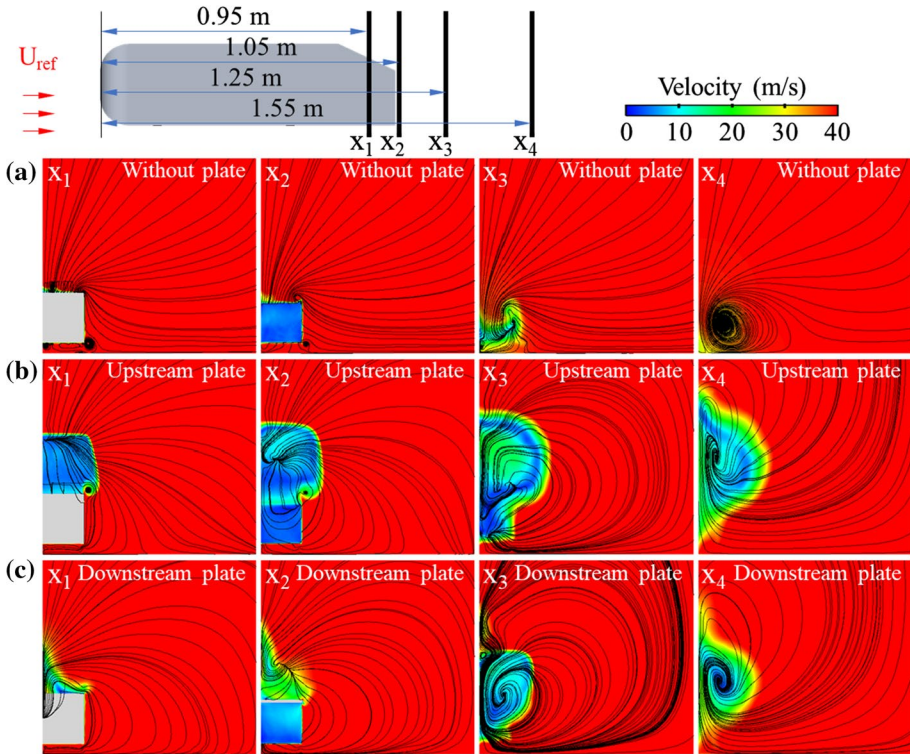


Fig. 7 Comparison of the velocity distribution and streamlines on the cross-sectional plane located at different positions (x_1 , x_2 , x_3 , and x_4) downstream of the Ahmed car with upstream plate **a** and downstream plate **b** at θ of 90°

5.2 Effect of Size and Opening Angle of on Aerodynamic Behaviour of Ahmed Car

As shown in Fig. 10a, as the θ increases, the C_x of the car body increases, irrespective of the installation position of the plate. However, for the upstream plate, as the C_x of the car body approaches the maximum with increase of the θ , but the rate of increase of the C_x decreases significantly; For the downstream plate, the C_x of the car body increases linearly with the θ . However, the C_x is significantly greater than that of the downstream plate. Figure 10a also shows that the C_x of the upstream plate increases rapidly as the θ increases; at close to 90° , the C_x of the plate exceeds that of the car body. The C_x of the downstream plate increases first and then reduces with the θ of the plate, while the θ is approximately 50° , the C_x of the downstream plate is the largest. Figure 10b shows that the variation law for the C_z of the car body and θ is affected by the installation position of the plate, the C_z of the car body decreases with the θ of the upstream plate, but it is opposite for the downstream plate. Figure 10b also shows that the C_z of the downstream plate decreases with the θ of plate, and the C_z of the upstream plate decreases first and then increases with the θ of the plate, the turning point is around 70 degrees. As shown in Fig. 10c, the C_x of both car body and plate increases as the S_{plate} increases, the increase in the C_x of the plate is significantly greater than that of the car body. Figure 10c also shows that placing the upstream plate is optimal for improving the C_x of both car body and plate. Figure 10d

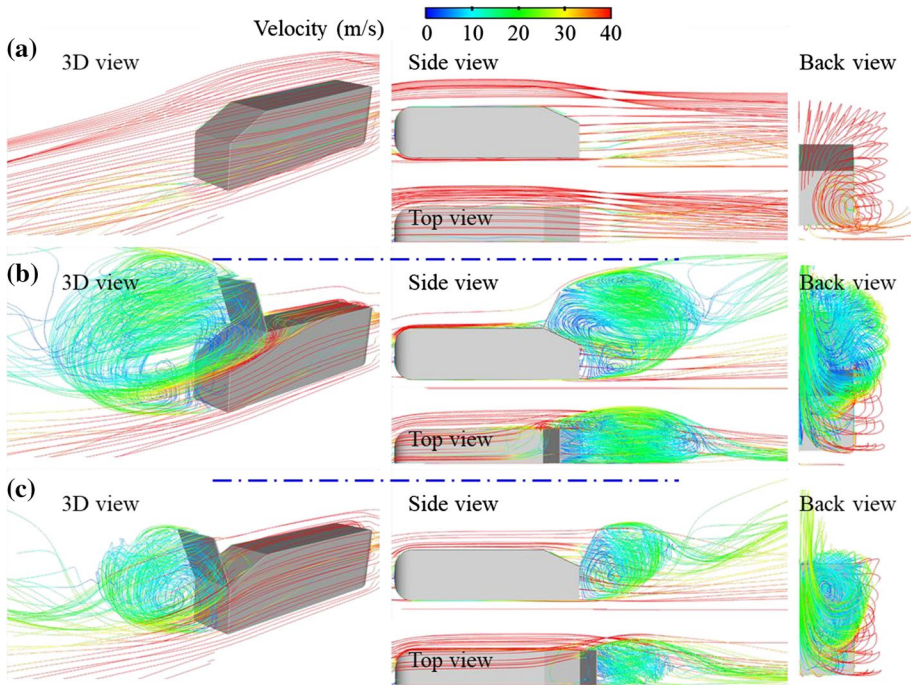


Fig. 8 3D streamlines around the car without plate **a**, with upstream plate **b** or downstream plate **c** at θ of 90°

shows that the C_z of both car body and plate increase with increasing S_{plate} . Setting the plate upstream of the slant back of the car helps to strengthen the downforce lift of the car body and plate, especially the car body, the above can further improve the contact friction between the wheel and the ground. This will be analyzed in combination with the flow field and explained later. Generally, the increase in the C_z of the car body is significantly greater than that of the plate, and the placing the plate upstream is better than placing it downstream with respect to the C_z of both the car body and plate.

As shown in left of Fig. 11, as the θ of the upstream plate increases, more of the wake is affected, and the airflow velocity in the wake decreases. As the θ of the upstream plate increase, a prominent vortex begins to form downstream of the upstream plate and gradually approaches the rear of the car, and the range of the vortex is also increased, which further increases the C_x of both car body and plate, which has been presented in Fig. 10a. When the θ of the upstream plate exceeds 70° , the vortex covers the whole rear of the car body, negative pressure of the flow field around the car rear and downstream of the upstream plate is further intensified, resulting in the reduction of the negative lift of the car body, which can be observed in Fig. 10b. As shown in right of Fig. 11, when the downstream plate is opened, a vortex appears in front of the plate, and the scale of vortex increases significantly as the θ of the downstream plate increases. The aforementioned phenomena are consistent with the variation law of aerodynamic coefficients and θ in Fig. 10a and b.

As shown in Fig. 12, as the S_{plate} decreases, the range of the disturbed area in the wake basically decreases. The range of disturbed area in the wake of the car with the

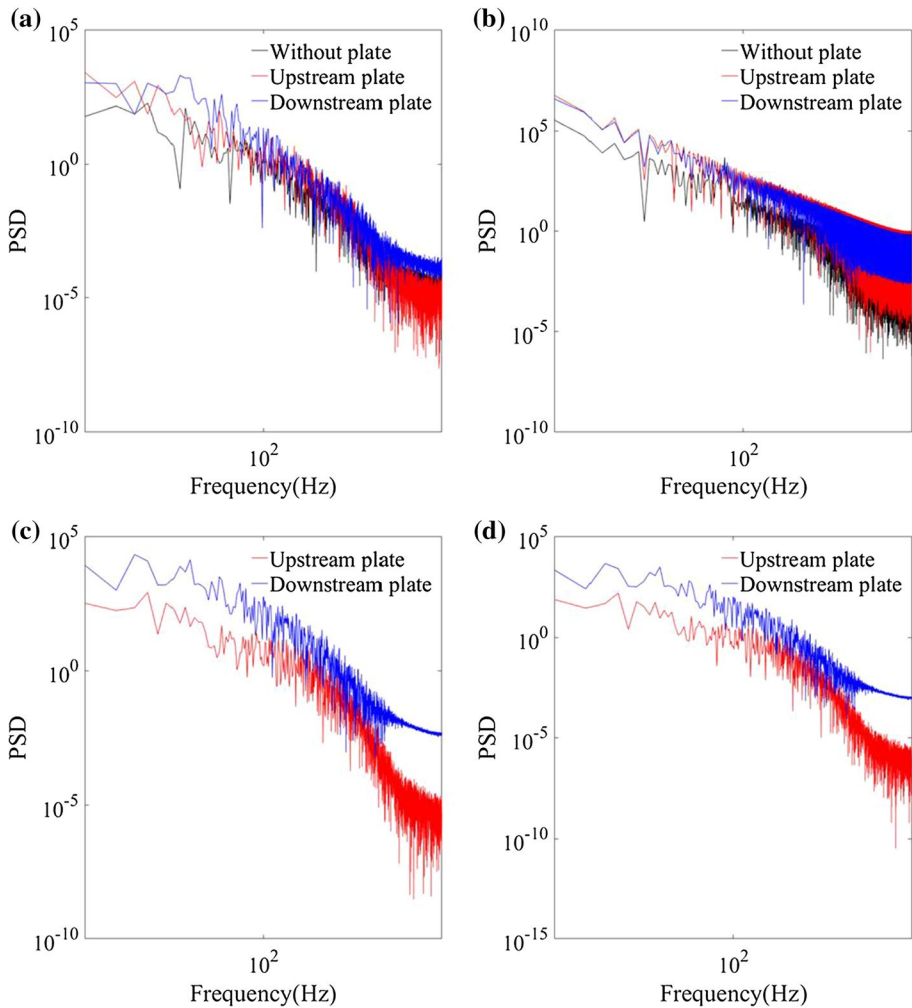


Fig. 9 PSD of aerodynamic coefficients (C_x and C_z) of the car with or without plate: **a** and **b** are for C_x and C_z of the car body, respectively; **c** and **d** are for C_x and C_z of the plates, respectively

upstream plate is significantly larger than that of the downstream plate, which may explain why the C_x of the car with upstream plate is greater than that of the downstream plate. When the height of downstream plate dropped below that of the upper surface of the car, the plate blocked the airflow detaching from the car roof less. The wake range was also significantly reduced, reducing the C_x of both the car body and downstream plate.

Figure 13 shows that the distribution law of a pair of vortices in the wake of the car with upstream plate is basically not changed by the opening angle. However, the pair of vortices in the wake tend to expand to both sides of the car when the plate is downstream; the flow field downstream the car is more turbulence. Because the downstream plate is closer to the wake, effect of downstream plate on vortices in the wake are significantly larger than those in the upstream plate.

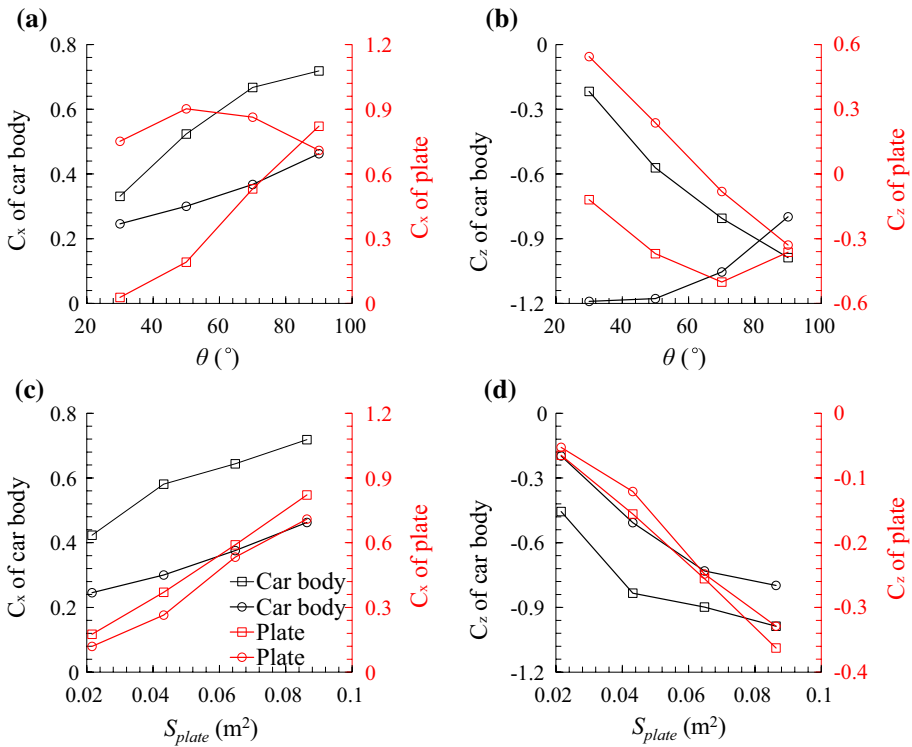


Fig. 10 Variation in aerodynamic coefficients of car body and plate in an Ahmed car with the size (S_{plate} , is from 0.22 m² to 0.86 m²) and opening angle (θ , is from 30° to 90°) of different plate configurations: **a** and **b** are for the cases with a full-size plate ($S_{plate} = 0.86$ m²), **c** and **d** are for the cases with a full-opening plate ($\theta = 90^\circ$). (\square and \circ are for the upstream and downstream plate, respectively.)

Figure 14 shows that the distribution law of a pair of vortices in the wake is unaffected by the plate size. The scale of a pair of vortices in the wake of the car with an upstream plate increases as the plate size decreases. The wake of the car with downstream plate is turbulence, and the relationship between the scale of the vortices pair in the wake of the car with a downstream plate and the plate size is not clear, but the scale of this pair of vortices is a little larger than that of the upstream plate, which also tends to expand to both sides of the car. The above phenomenon is related to the fact that the downstream plate is closer to the wake.

5.3 Braking Distance of the Car Under the Action of Plate

The braking distance is the most effective parameter for directly evaluating the effect of the aerodynamic braking plate on car braking. Previous studies have found that the relationship between the aerodynamic drag and lift force and the square of car speed is linear (Hucho and Sovran 1993; Katz 2006). Aerodynamic braking is only considered without other types of brakes, and the force model of the car under braking is expressed as follows (Broniszewski and Piechna 2019; Kurec et al. 2019a, 2019b):

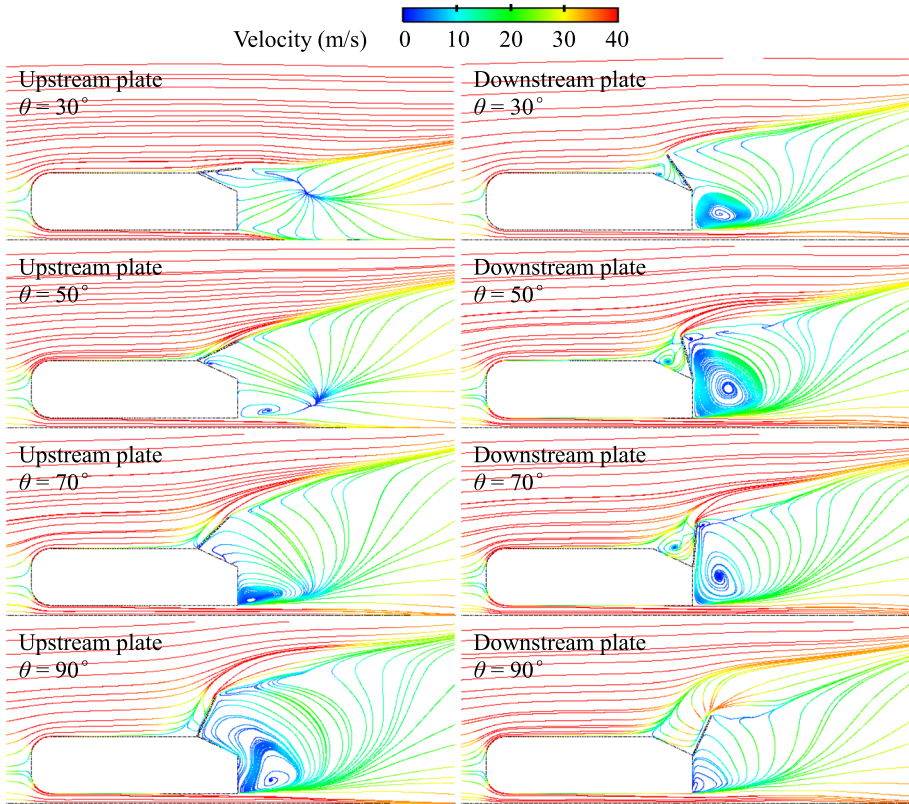


Fig. 11 Streamlines around the car with upstream and downstream plates with full-size ($S_{\text{plate}} = 0.086 \text{ m}^2$) at different opening angles (θ) on the symmetrical plane

$$m \frac{du}{dt} = \mu_{(t)} (mg - 0.5\rho u^2 AC_z) + 0.5\rho u^2 AC_x \tag{13}$$

where m and u are the car mass and car speed, respectively. The terms $\mu_{(t)}(mg - 0.5\rho u^2 AC_z)$ and $0.5\rho u^2 AC_x$ are the frictional drag and aerodynamic drag; g is the acceleration of gravity (considered to be 9.8 m/s^2 in this study); and $\mu_{(t)}$ is the dynamic friction coefficient.

The calculation formula for the braking distance, s , can be obtained by integrating formula (14) as follows:

$$s = \int_{U_{\text{min}}}^{U_{\text{max}}} \frac{mu \cdot du}{\mu_{(t)} (mg - 0.5\rho u^2 AC_z) + 0.5\rho u^2 AC_x} \tag{14}$$

where U_{max} and U_{min} are the maximum speed and minimum speed after braking, respectively. The mass of the car (m) is assumed to be approximately 16 kg for the 1/5th Ahmed car model, and the friction coefficient (μ) is 0.5 instead of $\mu_{(t)}$ to simplify the calculation model. The braking distances for the car with different plate configurations at different opening angles were calculated using Eq. (15), and the results are presented in Tables 3 and 4.

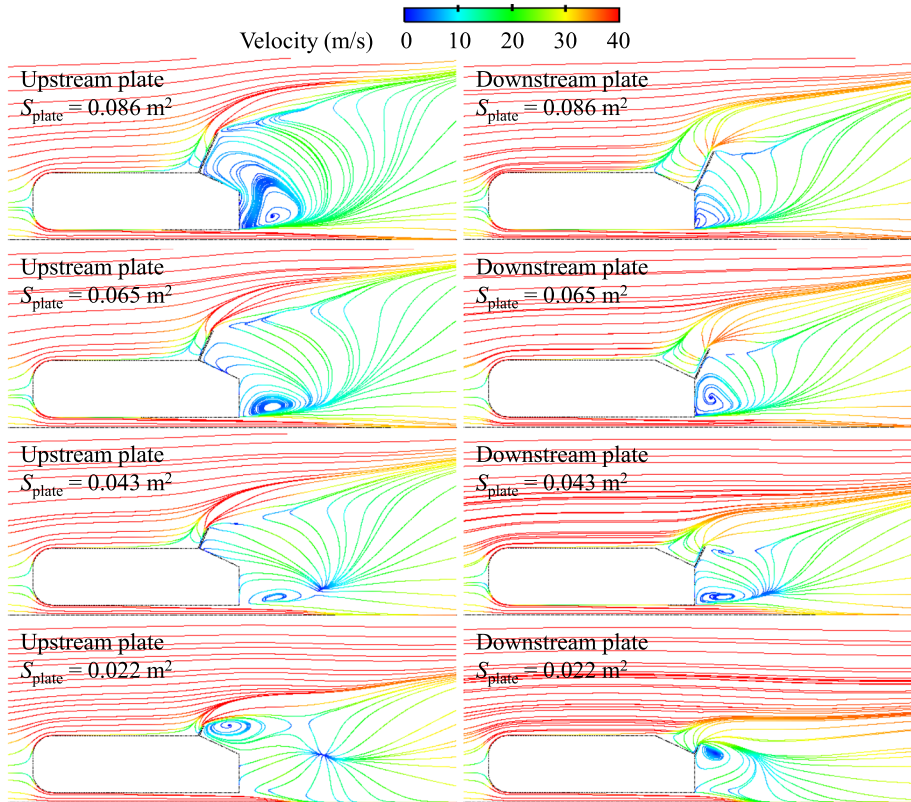


Fig. 12 Streamlines around the car with different size of plate configurations (S_{plate}) at full-opening angle ($\theta=90^\circ$) on the symmetrical plane

As shown in Table 3, the braking distance of the car with the upstream plate decreases as the opening angle increases (from 19 to 56%), and the effect of the opening angle on the braking distance of the car with upstream plate is more significant than that of the downstream plate. The good aerodynamic braking performance can be obtained when the opening angle of the downstream plate is small, but the braking effect improves slightly as the opening angle increases. The optimal opening angle of the downstream plate is approximately 70° . Table 4 shows that the braking distance of the car with upstream or downstream plates decreases as the plate size increases, and the effect of the upstream plate on the aerodynamic braking distance is markedly better than that of the downstream plate. When the downstream plate is small, the braking effect is not improved significantly, because the small plate cannot effectively block the air flow separated from the car roof. The aerodynamic forces used in this section are calculated according to the linear relationship between aerodynamic force and square of the car speed. The aerodynamic force coefficients used is obtained based on $U_{\text{ref}}=40$ m/s, which is greater than the calculated car speed range (22.22 m/s to 33.33 m/s). According to the law that the aerodynamic coefficient decreases with the car speed, the aerodynamic coefficients used in the calculation are relatively small compared with the real value. Therefore, the calculated value of braking distance in this paper is relatively small

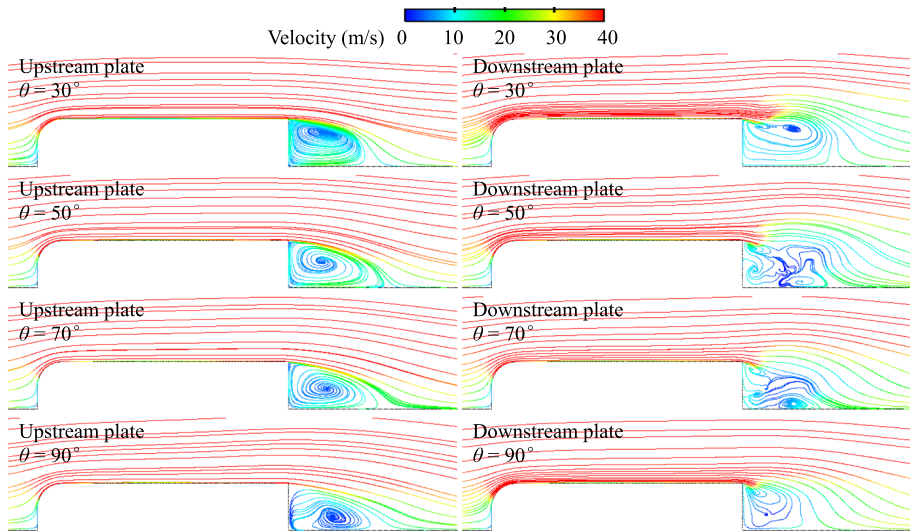


Fig. 13 Streamlines around the car with a full-size ($S_{\text{plate}} = 0.086 \text{ m}^2$) plates at different opening angles (θ) on the horizontal plane 0.15 m above the ground

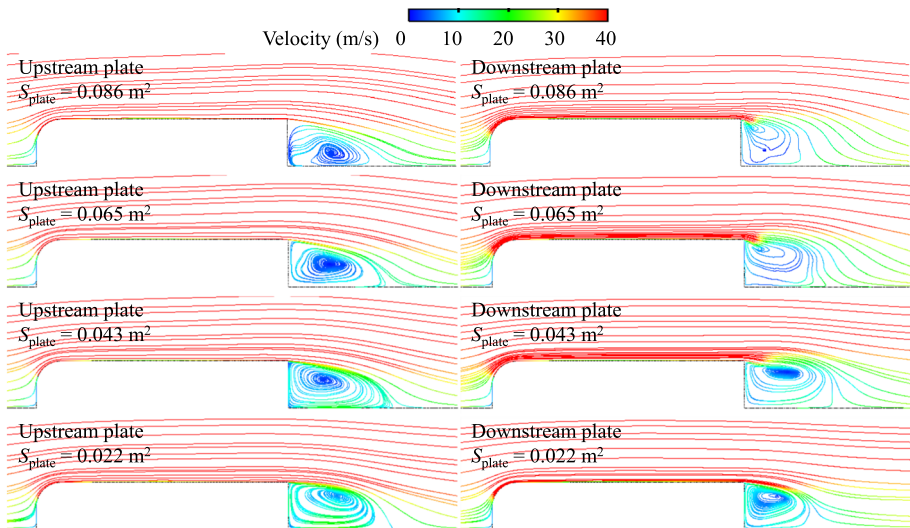


Fig. 14 Streamlines around the car with different size of plate configurations (S_{plate}) at a full-opening angle ($\theta = 90^\circ$) on the horizontal plane 0.15 m above the ground

compared with the real value. Because, at different speeds, the contact area between each tire and ground is different, which will cause the friction coefficient between the car and the ground to change from time to time, that is $\mu(t)$ changes all the time, and $\mu(t)$ adopted in this paper is fixed, which will also cause distortion of calculation results.

Table 3 Aerodynamic braking distances of the Ahmed car with plates at different opening angles and their differences from the base case (without plate)

Plate	U_{max} to U_{min} (km/h)	Braking distance (m)					Improvement (%)			
		Base	30°	50°	70°	90°	30°	50°	70°	90°
Upstream	120 to 80	56.74	46.12	34.73	27.82	25.11	19	39	51	56
Downstream			33.06	29.39	28.27	28.82	42	48	50	49

Table 4 Aerodynamic braking distances of the Ahmed car given multi-size plates at an opening angle of 90°, and their differences from the base case (without plate)

Plate	U_{max} to U_{min} (km/h)	Braking distance (m)					Improvement (%)			
		Base	1/4	1/2	3/4	1	1/4	1/2	3/4	1
Upstream	120 to 80	56.74	39.56	31.65	28.16	25.11	30	44	50	56
Downstream			47.00	39.22	32.16	28.82	17	31	43	49

6 Conclusions

The effects of installation position and opening angle on the aerodynamic behavior and aerodynamic braking distance of the car were studied and compared. The conclusions drawn from the obtained results are as follows:

1. Aerodynamic forces of the car with the upstream plate are significantly greater than those on the downstream plate. The aerodynamic drag is more sensitive to the installation position of the plate relative to the aerodynamic lift. Placing the plate upstream is optimal for increasing the car aerodynamic braking performance, and markedly reduces fluctuation in aerodynamic forces.
2. The C_x of the car body increases with the θ , which is not affected by position of the plate. The C_x of the downstream plate increases first and then reduces with the θ of the plate, while the θ is approximately 50°, the C_x of the downstream plate is the largest. The C_z of the car body decreases with the θ of the upstream plate, but it is opposite for the downstream plate. The C_z of the downstream plate decreases with the θ of plate, and the C_z of the upstream plate decreases first and then increases with the θ of the plate, the turning point is around 70 degrees. Placing the upstream plate is optimal for improving the C_x of both car body and plate. The C_z of both car body and plate increase with increasing S_{plate} .
3. Aerodynamic braking distance of the car decreases as the θ and S_{plate} of the plate increase, particularly with respect to the upstream plate. The optimal θ of the downstream plate is approximately 70°, and the braking effect is not significant because the height of the downstream plate is small.

The contact force between the tire and the ground and the real-time change in the friction coefficient will be considered in future studies. Further, calculating the braking distance by analyzing the effect of the plate on the contact force distribution between several tires and the ground during plate braking is necessary.

Acknowledgements The authors would like to thank Huadong Yao from Mechanics and Maritime Sciences, Chalmers University of Technology for his valuable input and support throughout this work.

Author contributions JN conceived the idea of the study; FJ and JN analysed the data; FJ, JN, RL, and YW interpreted the results; FJ wrote the paper; all authors discussed the results and revised the manuscript.

Funding This study was supported by the National Natural Science Foundation of China (52172359), Fundamental Research Funds for the Central Universities (XJ2021KJKZK010), Sichuan Science and Technology Program (2020JDTD0012), and Foundation of State Key Laboratory of Automotive Simulation and Control (20191104).

Declarations

Conflict of interest The authors declare that they have no conflict of interest.

References

- Ahmed, S., Ramm, G., Faltn, G.: Some salient features of the time-averaged ground vehicle wake. *SAE Trans.* **93**(2), 473–503 (1984)
- Ashton, N., Revell, A.: Key factors in the use of DDES for the flow around a simplified car. *Int. J. Heat Fluid Flow* **54**, 236–249 (2015)
- Ashton, N., West, A., Lardeau, S., Revell, A.: Assessment of RANS and DES methods for realistic automotive models. *Comput. Fluids* **128**, 1–15 (2016)
- Broniszewski, J., Piechna, J.: A fully coupled analysis of unsteady aerodynamics impact on vehicle dynamics during braking. *Eng. Appl. Comput. Fluid Mech.* **13**(1), 623–641 (2019)
- Conan, B., Jérme, A., Planquart, P.: Experimental aerodynamic study of a car-type bluff body. *Exp. Fluids* **50**(5), 1273–1284 (2011)
- Corallo, M., Sheridan, J., Thompson, M.C.: Effect of aspect ratio on the near-wake flow structure of an Ahmed body. *J. Wind Eng. Ind. Aerodyn.* **147**, 95–103 (2015)
- Devanuri, J.K.: Numerical investigation of aerodynamic braking for a ground vehicle. *J. Inst. Eng. (india) Ser. C* **99**(3), 329–337 (2018)
- Fares, E.: Unsteady flow simulation of the Ahmed reference body using a lattice Boltzmann approach. *Comput. Fluids* **35**(8–9), 940–950 (2006)
- Gritskevich, M., Garbaruk, A., Menter, F.: A comprehensive study of improved delayed detached eddy simulation with wall functions. *Flow Turbul. Combust.* **98**(2), 1–19 (2016)
- Guilmineau, E.: Computational study of flow around a simplified car body. *J. Wind Eng. Ind. Aerodyn.* **96**(6–7), 1207–1217 (2008)
- Guilmineau, E.: Effects of rear slant angles on the flow characteristics of the Ahmed body by IDDES simulations. *SAE World Congress Experience, Detroit, United States, Apr 2018* (2018). <https://doi.org/10.4271/2018-01-0720>
- Hucho, W., Sovran, G.: Aerodynamics of road vehicles. *Annu. Rev. Fluid Mech.* **25**(1), 485–537 (1993)
- Joseph, P., Xavier, A., Aider, J.: Drag reduction on the 25° slant angle Ahmed reference body using pulsed jets. *Exp. Fluids* **52**(5), 1169–1185 (2012)
- Katz, J.: Aerodynamics of race cars. *Annu. Rev. Fluid Mech.* **38**, 27–63 (2006)
- Krajnović, S., Davidson, L.: Flow around a simplified car, Part 1: large eddy simulation. *ASME J. Fluids Eng.* **127**(5), 907–918 (2005a)
- Krajnović, S., Davidson, L.: Flow around a simplified car, Part 2: understanding the flow. *J. Fluids Eng. Trans. ASME* **127**(5), 919–928 (2005b)
- Kudrauskas, N.: Analysis of emergency braking of a vehicle. *Transport* **22**(3), 154–159 (2007)
- Kurec, K., Remer, M., Mayer, T., Tudruj, S., Piechna, J.: Flow control for a car-mounted rear wing. *Int. J. Mech. Sci.* **152**, 384–399 (2019a)
- Kurec, K., Remer, M., Piechna, J.: The influence of different aerodynamic setups on enhancing a sports car's braking. *Int. J. Mech. Sci.* **164**, 105140 (2019b)
- Liang, X., Liu, H., Dong, T., Yang, Z., Tan, X.: Aerodynamic noise characteristics of high-speed train foremost bogie section. *J. Cent. South Univ.* **27**, 1802–1813 (2020)
- Lienhart, H., Becker, S.: Flow and turbulence structure in the wake of a simplified car model. *SAE Trans.* **112**(6), 785–796 (2003)

- McKay, N., Gopalathnam, A.: The effects of wing aerodynamics on race vehicle performance. *SAE Trans.* **111**(6), 2254–2263 (2002)
- Menter, F.R., Kuntz, M.: Adaptation of eddy-viscosity turbulence models to unsteady separated flow behind vehicles. In: McCallen, R., Browand, F., Ross, J. (eds.) *The Aerodynamics of Heavy Vehicles: Trucks, Buses, and Trains*, pp. 339–352. Springer, Berlin (2004)
- Minguez, M., Pasquetti, R., Serre, E.: High-order large-eddy simulation of flow over the “Ahmed body” car model. *Phys. Fluids* **20**(9), 095101 (2008)
- Mohammadikalakoo, B., Schito, P., Mani, M.: Passive flow control on Ahmed body by rear linking tunnels. *J. Wind Eng. Ind. Aerodyn.* **205**, 104330 (2020)
- Niu, J., Wang, Y., Zhou, D.: Effect of the outer windshield schemes on aerodynamic characteristics around the car-connecting parts and train aerodynamic performance. *Mech. Syst. Signal Process.* **130**, 1–16 (2019)
- Niu, J., Wang, Y., Wu, D., Liu, F.: Comparison of different configurations of aerodynamic braking plate on the flow around a high-speed train. *Eng. Appl. Comput. Fluid Mech.* **14**(1), 655–668 (2020a)
- Niu, J., Wang, Y., Liu, F., Chen, Z.: Comparative study on the effect of aerodynamic braking plates mounted at the inter-carriage region of a high-speed train with pantograph and air-conditioning unit for enhanced braking. *J. Wind Eng. Ind. Aerodyn.* **206**, 104360 (2020b)
- Niu, J., Wang, Y., Li, R., Liu, F.: Comparison of aerodynamic characteristics of high-speed train for different configurations of aerodynamic braking plates installed in inter-car gap region. *Flow Turbul. Combust.* **106**(1), 139–161 (2021a)
- Niu, J., Wang, Y., Liu, F., Li, R.: Aerodynamic behavior of a high-speed train with a braking plate mounted in the region of inter-car gap or uniform-car body: A comparative numerical study. *Proc. Inst. Mech. Eng. Part F J. Rail Rapid Transit* **235**(7), 815–826 (2021b)
- Niu, J., Wang, Y., Liu, F., Li, R.: Numerical study on the effect of a downstream braking plate on the detailed flow field and unsteady aerodynamic characteristics of an upstream braking plate with or without a crosswind. *Veh. Syst. Dyn.* **59**(5), 657–674 (2021c)
- Rao, A., Minelli, G., Basara, B., Krajnović, S.: On the two flow states in the wake of a hatchback Ahmed body. *J. Wind Eng. Ind. Aerodyn.* **173**, 262–278 (2018)
- Rossitto, G., Sicot, C., Ferrand, V., Borée, J., Harambat, F.: Influence of afterbody rounding on the pressure distribution over a fastback vehicle. *Exp. Fluids* **57**(3), 1–12 (2016)
- Serre, E., Minguez, M., Pasquetti, R., Guilmineau, E., Deng, G.B., Kornhaas, M., Rodi, W.: On simulating the turbulent flow around the Ahmed body: a French-German collaborative evaluation of LES and DES. *Comput. Fluids* **78**, 10–23 (2013)
- Spalart, P.: Comments on the feasibility of LES for wings, and on a hybrid RANS/LES approach. In: *Proceedings of first AFOSR international conference on DNS/LES*. Greyden Press (1997)
- Spalart, P., Deck, S., Shur, M., Squires, K., Strelets, M., Travin, A.: A new version of detached-eddy simulation, resistant to ambiguous grid densities. *Theoret. Comput. Fluid Dyn.* **20**(3), 181 (2006)
- Thacker, A., Aubrun, S., Leroy, A., Devinant, P.: Effects of suppressing the 3D separation on the rear slant on the flow structures around an Ahmed body. *J. Wind Eng. Ind. Aerodyn.* **107**, 237–243 (2012)
- Thacker, A., Aubrun, S., Leroy, A., Devinant, P.: Experimental characterization of flow unsteadiness in the centerline plane of an Ahmed body rear slant. *Exp. Fluids* **54**(3), 1479 (2013)
- Travin, A., Shur, M., Strelets, M., Spalart, P.R.: Physical and numerical upgrades in the detached-eddy simulation of complex turbulent flows. In: Friedrich, R., Rodi, W. (eds.) *Advances in LES of Complex Flows*, pp. 239–254. Springer, Dordrecht (2002)
- Xiao, Z., Fu, S.: Studies of the unsteady supersonic base flows around three afterbodies. *Acta. Mech. Sin.* **25**(4), 471–479 (2009)
- Zhai, Y., Niu, J., Wang, Y., Liu, F., Li, R.: Unsteady flow and aerodynamic behavior of high-speed train braking plates with and without crosswinds. *J. Wind Eng. Ind. Aerodyn.* **206**, 104309 (2020)
- Zuo, J., Wu, M., Tian, C., Xi, Y., Luo, Z., Chen, Z.: Aerodynamic braking device for high-speed trains: design, simulation and experiment. *Proc. Inst. Mech. Eng. Part F J. Rail Rapid Transit* **228**(3), 260–270 (2014)

Publisher's Note Springer Nature remains neutral with regard to jurisdictional claims in published maps and institutional affiliations.

Springer Nature or its licensor (e.g. a society or other partner) holds exclusive rights to this article under a publishing agreement with the author(s) or other rightsholder(s); author self-archiving of the accepted manuscript version of this article is solely governed by the terms of such publishing agreement and applicable law.